Photocatalysis
Research and Potential

SCIEPublish

Article

Chiral Aromatic Hydroxylamine-Coadsorbed TiO_2 Photocatalysts for Enantioselective Hydrogenation of Aromatic Ketones: Influence of Crystal Shapes and Facets

Akira Kawashima, Kaori Hanaie, Hideto Miyabe and Shigeru Kohtani *

Department of Pharmacy, School of Pharmacy, Hyogo Medical University, 1-3-6 Minatojima, Chuo-ku, Kobe 650-8530, Japan; ak-kawashima@hyo-med.ac.jp (A.K.); ph21080@hyo-med.ac.jp (K.H.); miyabe@hyo-med.ac.jp (H.M.)

* Corresponding author. E-mail: kohtani@hyo-med.ac.jp (S.K.)

Received: 15 February 2026; Revised: 19 March 2026; Accepted: 22 April 2026; Available online: 9 May 2026

ABSTRACT: Enantioselective photohydrogenation using semiconductor photocatalysts remains challenging because of the heterogeneity of solid surfaces and the difficulty in controlling adsorption geometries. In this study, we systematically investigated the enantioselective photohydrogenation of aromatic ketones using TiO_2 photocatalysts in the presence of chiral co-adsorbents, focusing on the combined effects of co-adsorbent structure and TiO_2 crystal morphology. Chiral aromatic amino alcohols, such as 2-amino-1-phenylethanol (PhEA), were identified as effective and relatively photostable co-adsorbents, affording moderate enantioselectivity with reduced inhibition compared with carboxylate-type co-adsorbents. Structural analyses revealed pronounced differences in particle size, lattice distortion, and inferred exposed crystal facets among anatase TiO_2 samples. TIO-13, composed of larger particles with relatively well-defined surface structures, exhibited higher and more reproducible enantioselectivity, whereas TIO-7, composed of smaller nanoparticles with more heterogeneous surfaces, showed higher reaction rates but lower enantioselectivity. Consecutive photohydrogenation experiments provided supportive evidence that residual surface-adsorbed chiral co-adsorbent contributes to both asymmetric induction and inhibition of the reaction. Although the present work should be regarded primarily as a fundamental study rather than a practically optimized catalytic methodology, it provides useful insight into the design of chiral semiconductor photocatalysts for heterogeneous asymmetric photocatalysis.

Keywords: Photocatalysis; Enantioselective photohydrogenation; TiO_2; Chiral co-adsorbents; Crystal facets; Surface structure

1. Introduction

The application of inorganic semiconductors to asymmetric photocatalysis has been actively investigated in recent years [1–4]. Titanium oxides (TiO_2) are one of the most extensively and in-depthly studied inorganic nanomaterials; thus, the development of chiral titanium oxides for achieving

enantioselective organic reactions is a challenging task. Photocatalysis can drive unique redox organic reactions that are not achievable with conventional techniques using oxidants or reductants. Therefore, the asymmetric photocatalysis using heterogeneous semiconductors is expected as a new method for the fine chemical synthesis of highly valuable molecules such as chiral medicines.

In 2010, we discovered that aromatic ketones could be quantitatively hydrogenated to secondary alcohols through photoreductive hydrogenation using TiO_2 [5]. This work demonstrated that ethanol acts as both the solvent and the sacrificial reagent, and that acetaldehyde is formed as the oxidation product of ethanol. In addition, our previous kinetic study showed that electrons accumulated at Ti electron trap sites after photoexcitation of TiO_2 are responsible for ketone reduction, and that the one-electron transfer from these trapped-electron sites to the adsorbed substrate is the rate-determining step of the overall reaction [6]. Furthermore, in 2018, we found that the coexistence of chiral hydroxylic acids, such as mandelic acid (MA), in the reaction system led to the enantioselective production of one enantiomer of the secondary alcohol [7]. This is mainly related to the adsorption of the carboxyl group of MA to the TiO_2 surface and the interaction between the aromatic ring of MA and adsorbed aromatic ketones on TiO_2. However, the addition of MA strongly inhibited the desired hydrogenation of ketones, resulting in low product yields. The hydrogenation reaction would be competitively suppressed by the strong adsorption of MA to the Ti reactive sites on the TiO_2 surface. Further, it was also observed that the enantiomeric excess (*ee*) of the secondary alcohols gradually decreased with the progress of this photohydrogenation reaction. The reason was found to be the decarboxylation of the carboxyl group of MA due to photo-Kolbe reaction involving the oxidation caused by the photogenerated holes of TiO_2 [7].

We have also reported the differences in reaction rate and enantioselectivity between anatase, rutile, and their mixed-phase TiO_2 photocatalysts [7]. The mixed-phase P25 and the anatase TIO-13 exhibited relatively high enantioselectivities, whereas the anatase TIO-7 and rutile showed low enantioselectivity. These results suggest that the TiO_2 crystal phase strongly influences enantioselectivity. Interestingly, anatase TIO-13 and TIO-7 exhibited completely different enantioselectivities, including the stereochemical inversion of the absolute configuration of secondary alcohol products, though these two TiO_2 powders are the same anatase crystalline phases. It should be noted in the transmission electron microscopy (TEM) images that P25 and TIO-13 possess larger particle sizes with smooth and flat surfaces, whereas TIO-7 has a smaller size with a significant amount of edges and corners and a larger specific surface area [7]. Up to now, there are still many unknowns and uncertainties regarding the stereoselective reaction on TiO_2 crystal surfaces.

TiO_2 exhibits different stability and photocatalytic activity depending on the surface structure (atomic arrangement) of the crystal planes, even within the same crystalline phase [8]. For example, the anatase phase has the {101} facet, which is known to have the most stable surface energy and is most susceptible to photoreductive reactions [9,10], the {001} facet, which has attracted attention for its unstable but high oxidation reactivity [9,10]; and the {112} facet, which has recently attracted attention for its high chemical reactivity [11]. Each crystal facet has a different atomic arrangement and lattice defects, and the different surface energies result in different accumulations of photogenerated electrons and holes. This has led to extensive discussions on which facets are more favorable for reduction or oxidation reactions. However, it is intriguing to speculate that the differences in the atomic arrangement of the crystal planes cause differences in the interactions between substrates adsorbed on these surfaces and chiral co-adsorbents, resulting in completely different enantioselectivities.

In this study, chiral aromatic hydroxylamines such as 2-amino-1-phenylethanol (PhEA) and 2-phenylglycinol (PhGly) were used instead of MA as chiral co-adsorbents. The reaction yields and enantioselectivities were evaluated in the photoreduction of 1′-acetonaphthone (1NP, **1a**) or 2′-acetonaphthone (2NP, **2a**) to 1-(1-naphthyl)ethanol (1NPOH, **1b**) or 1-(2-naphthyl)ethanol (2NPOH, **2b**) by comparing the results using MA, as shown in Scheme 1. Furthermore, the exposed crystal surfaces of two types of anatase-type TiO_2 (TIO-13 and TIO-7) were characterized in detail using X-ray diffraction

(XRD) analysis and high-resolution scanning transmission electron microscopy (STEM). As a result, a reasonable interpretation will be proposed and discussed to explain the relationship between the crystal structure of TiO_2 and enantioselective photohydrogenation of aromatic ketones with chiral co-adsorbents PhEA or MA on the TiO_2 surface.

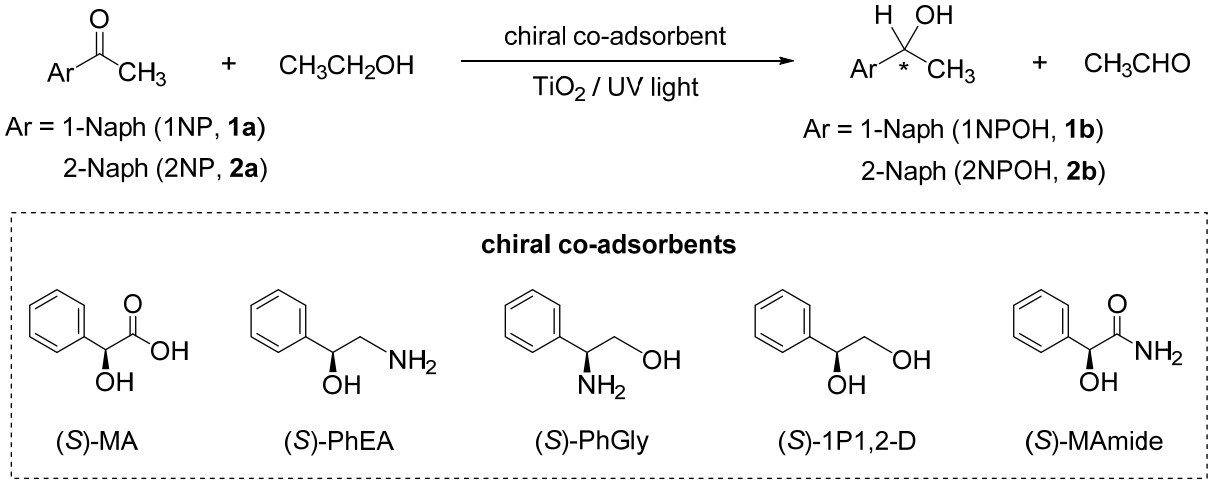

Scheme 1. Enantioselective photohydrogenation of aromatic ketones **1a** and **2a** with the chiral co-adsorbents on TiO_2. The asterisk (*) shown in the structural formulas of products **1b** and **2b** indicates a chiral carbon.

2. Materials and Methods

2.1. Materials

Polycrystalline TiO_2 powder (Degussa P25) was purchased from Japan Aerosil and used as received. Rutile TiO_2 powder (TIO-6) and anatase TiO_2 powders (TIO-7 and TIO-13) were supplied as reference photocatalysts by the Catalysis Society of Japan. The crystalline phases of these TiO_2 samples were confirmed by XRD measurements using a D6 PHASER (Bruker AXS GmbH, Karlsruhe, Germany) equipped with a Cu Kα radiation source (λ = 0.15418 nm). The crystallite sizes were estimated from the XRD patterns using the Scherrer equation. The anatase/rutile ratio of P25 was approximately 8/2, as determined by XRD analysis. TEM observations were carried out using a JEOL JEM-1400Plus microscope (JEOL Ltd., Tokyo, Japan) operated at an accelerating voltage of 80 kV. STEM observations were performed using a JEOL JEM-ARM200F microscope (JEOL Ltd., Tokyo, Japan) operated at an accelerating voltage of 200 kV. For TEM and STEM observations, TiO_2 powders were dispersed in ethanol by ultrasonication and drop-cast onto carbon-coated copper grids, followed by vacuum drying prior to observation.

The following reagents were used for substrates and chiral co-adsorbents as received: 1′-acetonaphthone (1NP, TCI, >98.0%), 2′-acetonaphthone (2NP, TCI, >98.0%), (*S*)-(−)-1-(1-naphthyl)ethanol ((*S*)-1NPOH, Aldrich, 98%), (*S*)-(−)-1-(2-naphthyl)ethanol ((*S*)-2NPOH, Aldrich, 98%), 1-(1-naphthyl)ethanol (1NPOH, racemic mixture, TCI, 98%), 1-(2-naphthyl)ethanol (2NPOH, racemic mixture, TCI, 98%), L-(+)-mandelic acid ((*S*)-MA, TCI, >99.0%), (*S*)-(+)-1-phenylethan-1,2-diol ((*S*)-1P1,2D, TCI, >98%), (*S*)-mandelamide ((*S*)-MAmide, BLD pharm, >95%), (*S*)-2-Phenylglycinol ((*S*)-PhGly, Combi-Blocks, >98%), (*S*)-2-Amino-1-phenylethanol ((*S*)-PhEA, Combi-Blocks, >98%). Specially reagent grade of ethanol and methanol were purchased from Nacalai Tesque and used for a solvent in photocatalytic reactions and eluent on a high performance liquid chromatography (HPLC) without further purification.

2.2. Photoirradiation Experiment

All irradiation experiments were carried out as denoted in the previous report [7]. Mixtures of aromatic ketones (0.13 mmol) and TiO_2 (0.10 g) were dispersed in the presence or absence of chiral reagents (0.25

mmol) in ethanol solution (25 mL). The solutions were placed in a cylindrical glass cell (40 mm × 45 mm i.d.) and sealed with a rubber septum. Argon gas (99.99%) was passed into the solutions through the rubber septum for 30 min, and then the degassed solutions were stirred in a water bath for 30 min to attain thermal equilibrium at 32 °C in the dark. The suspended solutions were irradiated with UV light (wavelength >350 nm) from a 300 W xenon arc lamp (CERMAX LX300, ILC Technology, Sunnyvale, CA, USA) through a dichroic mirror and a cut-off filter (UV-35, Toshiba Corp., Tokyo, Japan). Light intensity was measured to be 720 mW·cm^{-2} by the use of a thermopile sensor (Model 210, Coherent Inc., Santa Clara, CA, USA). After appropriate irradiation times, 0.2 mL of the sample solution was withdrawn and centrifuged to remove the photocatalyst powders. Concentrations of the substrates and products in supernatants were determined using an HPLC system equipped with UV detection (PU-2080 pump, DG-2080-35 degasser, CO-2065 column oven, and UV-2075 UV/vis detector; JASCO Corp., Tokyo, Japan). A reverse-phase system with a chiral column (Daicel Chiralcel OD-RH, 150 mm × 4.6 mm i.d.) was used to analyze the substrates and products. A mobile phase was methanol/water (3/1, *v*/*v*) with a flow rate of 0.7 mL/min. Chromatograms were monitored at 286 nm. From the results, yields and enantiomeric excesses (*ee*) of the products were calculated, where the sign of *ee* was defined so that a positive value was obtained when the *R*-isomer of the product was in excess. Furthermore, when a chiral co-adsorbent is present in the solution, the co-adsorbent adsorbs onto the Ti sites on the TiO_2 surface, resulting in the inhibition of the reaction. Therefore, we defined the inhibition ratio (*IR*) as below [7]:

$$IR(\%)=\left(1-\frac{r}{r_0}\right)\times 100$$

where r and r_0 are the initial reaction rates during 0–5 h irradiation in the presence and absence of chiral reagents, respectively.

3. Results and Discussion

3.1. Enantioselective Photohydrogenation on P25 TiO_2

We firstly investigated the enantioselective photohydrogenation of **1a** and **2a** in the presence of several chiral co-adsorbents on P25 TiO_2, because this TiO_2 has been extensively studied as a benchmark for TiO_2 photocatalysis. Table 1 summarizes yields and %*ee* of the products **1b** and **2b,** and *IR* (%) values when the *S*-isomers of the five chiral co-adsorbents were used. The use of (*S*)-MA shows the very low reaction yield even after 23 h and the high *IR* values 100% and 99% for **1b** and **2b**, respectively. This should be due to the inhibition of the hydrogenation reaction by the strong MA adsorption on the reactive sites of TiO_2 as reported previously [7]. Enantioselectivities +36%*ee* and +19%*ee* were observed after 5 h for **1b** and **2b**, respectively, but the %*ee* values decreased after 23 h when (*S*)-MA was used as a co-adsorbent. This is caused by the decomposition of MA in the decarboxylation of the carboxyl group of MA due to the photo-Kolbe oxidation reaction caused by the photogenerated holes on TiO_2 [7].

The use of (*S*)-PhEA as a co-adsorbent resulted in the reversal of the absolute configuration of **1b** and **2b** compared to the photohydrogenation using (*S*)-MA. Enantioselectivities of −13%*ee* for **1b** and −10%*ee* for **2b** were observed; these %*ee* values decreased slightly between 5 and 23 h. It should be noted that the high reaction yields of 69% for **1b** and 73% for **2b** were obtained after 23 h of irradiation. This is attributed to the resistivity against decomposition of (*S*)-PhEA during the photocatalytic reaction. Figure S1 shows the time profile of ($C/C_0 \times 100$), where C and C_0 are concentrations of (*S*)-PhEA at each reaction time and 0 h, respectively, during the photoreaction of **2a** to **2b**. Thus, unlike MA, PhEA is a relatively stable chiral coadsorbent during the photoirradiation. In the case of (*S*)-PhGly, the yields of **1b** and **2b** were slightly increased, although the enantioselectivities were dramatically decreased. Both (*S*)-PhEA and (*S*)-PhGly would adsorb to the Ti sites on TiO_2 through the amino and/or hydroxy groups as depicted in Figure 1. The

difference in enantioselectivity implies that the π-π interaction between (*S*)-PhEA and the aromatic rings of substrates **1a** and **2a** is in a more favorable configuration (**[A]** in Figure 1) than that between (*S*)-PhGly and **1a** and **2a** (**[B]** in Figure 1).

Table 1. Enantioselective photohydrogenation of **1a** and **2a** on P25 [a] TiO_2 after 5 and 23 h irradiation [b].

Chiral Co-Adsorbent	Time (h)	1a			2a		
		Yield (%)	%*ee* [c]	*IR* (%) [d]	Yield (%)	%*ee* [c]	*IR* (%) [d]
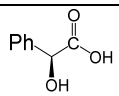 (*S*)-MA	5	0	+36	100	0	+19	99
	23	1	+26		3	+8	
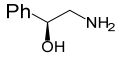 (*S*)-PhEA	5	11	−13	91	21	−10	86
	23	69	−8		73	−8	
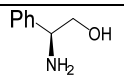 (*S*)-PhGly	5	34	+3	77	48	racemic	73
	23	99	+2		100	racemic	
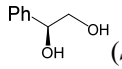 (*S*)-1P1,2D	5	53	racemic	59	70	racemic	28
	23	100	racemic		100	racemic	
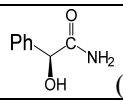 (*S*)-MAmide	5	—	—	—	72	racemic	26
	23	—	—		100	racemic	

[a] Mixture of anatase/rutile (ca. 8/2). [b] Carried out for a mixture of aromatic ketones (65 μmol), chiral reagents (250 μmol) and TiO_2 (0.10 g) in deaerated ethanol solution (25 mL) under the irradiation with UV light (>350 nm) at 303 K. [c] Defined by the following equation: %*ee* = 100([*R*] − [*S*])/([*R*] + [*S*]) where [*R*] and [*S*] are concentration of enantiomers of **1b** or **2b**. [d] Defined by the following equation: *IR* (%) = 100 × (1 − (r/r_0)) where r and r_0 are the initial reaction rates during 0–5 h irradiation in the presence and absence of chiral reagents, respectively.

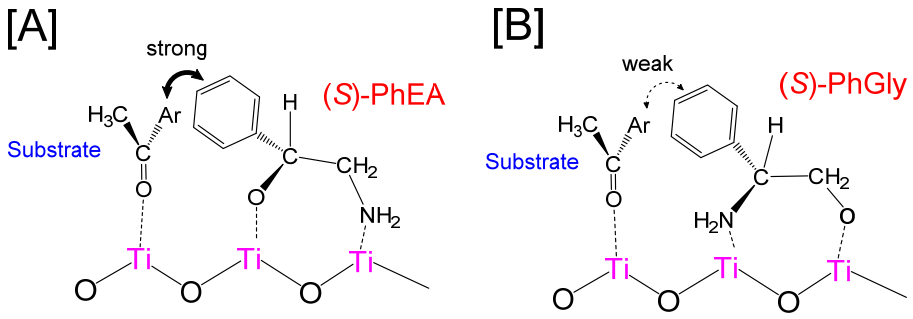

Figure 1. Schematic, hypothetical models for adsorption of **[A]** (*S*)-PhEA and **[B]** (*S*)-PhGly, and interaction between aromatic ketone and the co-adsorbents on the TiO_2 surface.

The *IR* values on the use of (*S*)-PhEA and (*S*)-PhGly were relatively high (approximately 70–90%), indicating strong adsorption of these amino alcohol-type co-adsorbents on the TiO_2 surface. The strong interaction of amino groups with TiO_2 surfaces has been demonstrated by in situ infrared spectroscopy, which indicates preferential adsorption of amine species on surface Ti sites [12]. This experimental evidence supports the interpretation that amino-containing co-adsorbents can strongly bind to TiO_2 surfaces and effectively influence the adsorption configuration of substrate molecules during photohydrogenation reactions. To provide supportive insight into the adsorption behavior of amino alcohol-type co-adsorbents, density functional theory calculations were performed using Gaussian to optimize molecular geometries and evaluate charge distributions. The calculated results indicate that the nitrogen atom of the amino group carries a more negative charge than the oxygen atom of the hydroxy group (Figure S2), suggesting a stronger interaction between the amino group and surface Ti sites. This electronic characteristic is consistent with the experimentally observed strong adsorption and high inhibition ratios for (*S*)-PhEA, as well as its higher stability under photoirradiation compared with carboxylate-type co-adsorbents such as MA. In contrast, (*S*)-1P1,2D, which contains two hydroxy groups but lacks a basic nitrogen atom, and (*S*)-

MAmide, bearing an amide substituent, exhibited no enantioselectivity and relatively low *IR* values. These results mean that the lone pair of the basic nitrogen atom on PhEA and PhGly plays an important role in the adsorption of these co-adsorbents to the Ti sites on the TiO_2 surface. Consistent with this interpretation, Parameswari et al. have reported that monoethanolamine ($HOCH_2CH_2NH_2$) adsorbed at five-coordinated Ti sites (probably the main reaction site) on rutile TiO_2 (110) through the strong interaction of the nitrogen atom of the amine group by the use of the density functional theory and *ab initio* molecular dynamics simulations [13]. Similar to the rutile TiO_2, the nitrogen atom of (*S*)-PhEA is likely to interact with five-coordinate Ti sites on the surface of anatase TiO_2, which may contribute to asymmetric induction, although the adsorption geometry shown in Figure 1 remains hypothetical.

3.2. Enantioselective Photohydrogenation on Several TiO_2 Powders

Next, we investigated the effect of TiO_2 crystal form on the enantioselective hydrogenation of **1a** and **2a** using four TiO_2 photocatalysts: mixed-phase P25, anatase TIO-13 and TIO-7, and rutile TIO-6. Table 2 summarizes the results when (*S*)-MA and (*S*)-PhEA were used as chiral co-adsorbents. For anatase TIO-13, a large enantiomeric excess of 73%*ee* was obtained in the hydrogenation of **1a**, although the yield was only 1% when (*S*)-MA was used. In the hydrogenation of **2a**, the yield of **2b** in 1% was obtained, but showed low *ee* (+20%*ee*). The use of (*S*)-PhEA instead of (*S*)-MA improved the reaction yields of **1b** and **2b** and exhibited moderate enantiomeric excess of −23%*ee* for **1b** and −20%*ee* for **2b** on TIO-13. On the other hand, for anatase TIO-7, the use of both (*S*)-PhEA and (*S*)-MA showed higher yields but lower enantiomeric excess of **1b** and **2b** than those on TIO-13. Notably, as previously reported [7], when (*S*)-MA was used, the product **2b** showed opposite stereoselectivity (−3%*ee*), and the product **1b** indicated racemate. This unique feature of TIO-7 may be due to its small crystallite size (<10 nm) and surface structure, which will be discussed in Sections 3.3 and 3.4. For rutile TIO-6, when the use of (*S*)-PhEA showed relatively high yields but low enantioselectivity. These results suggest that anatase TIO-13 and mixed-phase P25 are more favorable for asymmetric induction than anatase TIO-7 and rutile TIO-6 under the present reaction conditions.

To further examine whether enantioselectivity is associated with the adsorption of the chiral co-adsorbent on the TiO_2 nanocrystal surface, consecutive photohydrogenation experiments were performed (Figure S3, Table S1). First, an enantioselective photohydrogenation reaction was carried out in an ethanol solution (25 mL) containing the TiO_2 photocatalyst (TIO-13), the substrate (2NP), and the chiral co-adsorbent ((*S*)-PhEA) (1st irradiation). After the reaction, the suspension was centrifuged, and the supernatant was removed. Subsequently, a fresh ethanol solution (25 mL) containing only the substrate (2NP) was added to the recovered TiO_2, and the reaction was continued under photoirradiation (2nd irradiation). Since no additional co-adsorbent was introduced during the 2nd irradiation, the reaction yield increased compared with that in the 1st irradiation. Nevertheless, a small but detectable enantioselectivity was still observed at the early stage of the 2nd irradiation (e.g., 2.8%*ee* after 1 h), indicating that residual co-adsorbent adsorbed on the TiO_2 surface remained catalytically relevant. The *IR* during the 2nd irradiation was 51%, which, although lower than that in the 1st irradiation, still indicates appreciable suppression of the reaction. Notably, the *ee* value gradually decreased during the 2nd irradiation and eventually disappeared, which may be reasonably attributed to the gradual desorption of surface-adsorbed (*S*)-PhEA into the ethanol solution containing only 2NP. These results provide supportive, indirect evidence that the chiral co-adsorbent remaining on the TiO_2 surface contributes to both asymmetric induction and inhibition of the photohydrogenation reaction.

Table 2. Enantioselective photohydrogenation of **1a** and **2a** on each TiO_2 crystalline sample with (*S*)-MA or (*S*)-PhEA after 23 h irradiation [a].

TiO_2	**1b**						**2b**					
	(*S*)-MA			**(*S*)-PhEA**			**(*S*)-MA**			**(*S*)-PhEA**		
	Yield (%)	**%*ee* [b]**	***IR* [c] (%)**	**Yield (%)**	**%*ee* [b]**	***IR* [c] (%)**	**Yield (%)**	**%*ee* [b]**	***IR* [c] (%)**	**Yield (%)**	**%*ee* [b]**	***IR* [c] (%)**
P25	1	+26(*R*)	100	69	−8(*S*)	91	3	+8(*R*)	99	73	−8(*S*)	86
TIO-13	1	+73(*R*)	97	14	−23(*S*)	87	1	+20(*R*)	99	35	−20(*S*)	82
TIO-7	20	racemic	88	39	−13(*S*)	81	58	−3(*S*)	80	73	−11(*S*)	80
TIO-6	3	+10(*R*)	98	50	−3(*S*)	67	2	+8(*R*)	99	68	racemic	81

[a] Carried out for a mixture of aromatic ketones (65 μmol), chiral reagents (250 μmol) and TiO_2 (0.10 g) in deaerated ethanol solution (25 mL) under the irradiation with UV light (>350 nm) at 305 K. [b] Defined by the following equation: $\%ee = 100 \times ([R] - [S])/([R] + [S])$ where [*R*] and [*S*] are concentration of enantiomers of **1b** or **2b**. [c] Defined by the following equation: $IR\ (\%) = 100 \times (1 - (r/r_0))$ where r and r_0 are the initial reaction rates during 0–5 h irradiation in the presence and absence of chiral reagents, respectively.

3.3. Structural Characterization of TIO-7 and TIO-13 by XRD and TEM

The structural characteristics of TIO-7 and TIO-13 were examined by XRD measurements (Figure 2) and TEM observations (Figure S4) to clarify differences in particle size, morphology, and exposed crystal facets. In addition, STEM observations were performed for anatase TIO-7 and TIO-13 powders (Figure 3). The crystallite sizes estimated from XRD patterns using the Scherrer equation, average particle sizes obtained from TEM observations, and reported specific surface areas are summarized in Table 3.

The XRD patterns of all TiO_2 samples were consistent with previously reported crystal structures. Although both TIO-7 and TIO-13 possess the anatase phase, the diffraction peaks of TIO-7 were significantly broader than those of TIO-13, reflecting the smaller crystallite size of TIO-7. Moreover, differences in relative peak intensities suggest variations in crystal morphology and preferentially exposed facets between these two samples. Distinct physicochemical properties of TIO-7 and TIO-13, including differences in particle size and electronic characteristics, have also been reported previously [14]. Bertolotti et al. reported simulations of X-ray scattering patterns for bipyramidal anatase nanocrystals with predominantly exposed stable {101} facets, demonstrating that changes in the aspect ratio along the *a*- and *c*-axes significantly affect the diffraction profiles [15]. In the present study, the XRD patterns were deconvoluted based on the characteristic anatase peak positions, and the integrated peak areas were compared. When being normalized by the peak area of the {200} reflection ($2\theta = 48.0°$), corresponding to the *a*-axis direction, the area ratios of the {004} reflection ($2\theta = 37.8°$), corresponding to the *c*-axis direction, and the {220} reflection ($2\theta = 70.3°$), corresponding to the diagonal direction in the *ab* plane, were $S_{004}/S_{200} = 68.4$ and $S_{220}/S_{200} = 23.6$ for TIO-13. In contrast, these ratios decreased to $S_{004}/S_{200} = 54.7$ and $S_{220}/S_{200} = 19.6$ for TIO-7 (Table S2), suggesting a truncated morphology with less well-defined crystal edges and corners. These results are consistent with the TEM observations: TIO-13 exhibits a morphology close to a decahedral structure, whereas TIO-7 consists of much smaller, nearly spherical nanoparticles (Figures 3, S4 and S5). Accordingly, TIO-13 is expected to predominantly expose relatively stable {101} and {001} facets, while TIO-7 likely exposes a variety of facets induced by lattice distortion. For rutile TIO-6, the crystal structure corresponds to the rutile phase, and the nanocrystals are expected to grow preferentially along the *c*-axis [16], forming rod-like morphologies with {110} facets on the side surfaces and {101} facets at the terminal ends (Figure S4).

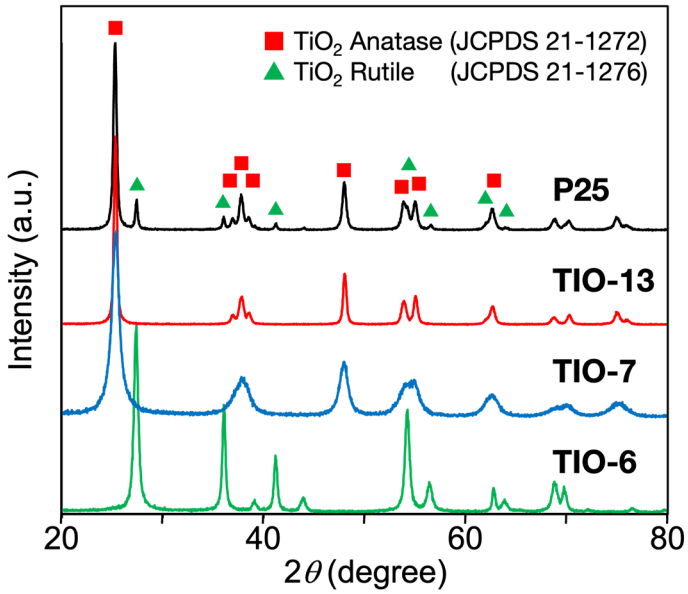

Figure 2. XRD patterns of TiO_2 powders (P25, TIO-13, TIO-7, and TIO-6). The positions of the characteristic diffraction peaks of anatase and rutile phases, based on JCPDS reference data (No. 21-1272 and No. 21-1276), are indicated by squares (■) and triangles (▲), respectively.

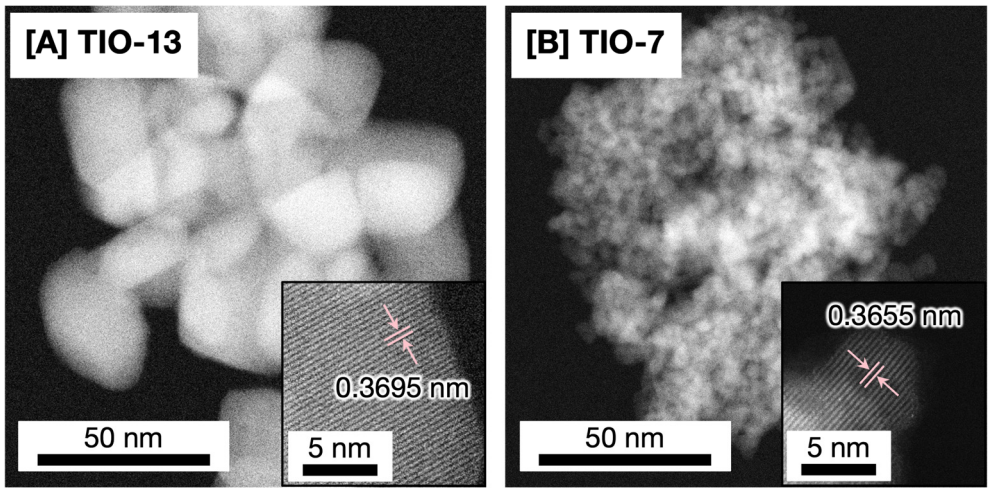

Figure 3. STEM images of anatase TiO_2 powders: **[A]** TIO-13 and **[B]** TIO-7. Insets show magnified views of the lattice fringes, from which the interplanar spacings were measured.

Table 3. Crystalline phase, crystallite size estimated from XRD patterns, average particle size measured from TEM images, and specific surface area of TiO_2 powders used in this study.

TiO_2	Crystalline Phase	Crystallite Size (nm) [a]	Average Particle Size (nm) [d]	Specific Surface Area (m^2/g)
P25	anatase/rutile (ca. 8/2)	20 [b]/35 [c]	21.5	61 [g]
TIO-13	anatase	22	23.9	59 [h]
TIO-7	anatase	9	6.0	270 [h]
TIO-6	rutile	19	15.2 [e]/46.4 [f]	100 [h]

[a] Estimated from XRD by using Scherrer equation. [b] For anatase, [c] for rutile. [d] Determined from TEM images. For rutile TIO-6, particle sizes along the [e] short and [f] long axis are listed due to its rod-like morphology. [g] From ref. [17]. [h] From ref. [18].

The lattice fringe spacings measured from the STEM images further support these structural differences (Figure 3). For TIO-13, lattice fringes with an interplanar spacing of 0.3695 nm were observed, which is close to the reported spacing of the anatase {101} planes (0.3516 nm). In the case of TIO-7, lattice

fringes with a spacing of 0.3655 nm were also observed, together with atomic arrangements and spot spacings consistent with the bulk-terminated anatase {112} planes, suggesting partial exposure of the {112} facets (Figure S6). The interplanar spacings were measured directly from the lattice fringes observed in the STEM images. Notably, the measured spacings were slightly larger than those expected from the ideal anatase lattice, indicating lattice distortion in the nanocrystals.

3.4. Relationship Between Crystal Structure and Enantioselective Photohydrogenation

The structural differences described above are closely related to the photocatalytic performance and enantioselectivity observed in the photohydrogenation reactions. The smaller particle size of TIO-7 results in a larger specific surface area compared with that of TIO-13. Consequently, in the absence of a chiral co-adsorbent, TIO-7 exhibits a higher reaction rate than TIO-13 (Table S3). Moreover, TIO-7 consistently shows the lowest inhibition ratios among all TiO_2 samples for all substrates and chiral co-adsorbents investigated (Table 2). In addition, the presence of multiple exposed facets may further enhance the catalytic activity of TIO-7. Joutsuka et al. reported that the anatase {112} facets exhibit high adsorption ability and photocatalytic degradation activity based on methylene blue experiments and density functional theory calculations [11]. If TIO-7 indeed exposes such {112} facets, this feature may contribute to its enhanced photohydrogenation activity. Differences in adsorption behavior and surface reactivity depending on the exposed crystal facets of anatase TiO_2 have been reported, particularly between the thermodynamically stable {101} facets and other facets such as {001} [19].

In contrast, the enantioselectivity was lower for TIO-7 than for TIO-13, showing an inverse relationship with the reaction rate. This behavior is reasonably interpreted in terms of the small particle size and large lattice distortion of TIO-7. Our previous studies demonstrated that effective enantioselective photohydrogenation requires chiral co-adsorbents bearing (i) a substituent that strongly binds to the TiO_2 surface, as well as (ii) a hydroxy group and (iii) a phenyl group directly attached to the chiral carbon center [7]. The presence of these three functional groups in the chiral co-adsorbent enables favorable interactions with the substrate molecules on the TiO_2 surface, thereby enhancing enantioselectivity. However, the adsorption geometries shown in Figure 1 should be regarded as hypothetical models proposed to rationalize the observed catalytic behavior, rather than as experimentally established structures.

When the particle size decreases and lattice distortion increases, as in the case of TIO-7, the distance between surface Ti adsorption sites is expected to expand, which can weaken the cooperative interactions between the chiral co-adsorbent and the substrate molecules. As a result, the enantioselectivity tends to decrease. Furthermore, the inversion of enantioselectivity observed for the photohydrogenation of **2a** on TIO-7 in the presence of (*S*)-MA may also be rationalized. While a fixed spatial arrangement between the adsorbed chiral co-adsorbent and the substrate would normally favor hydrogen addition from a specific direction, lattice distortion can increase the spacing between adjacent chiral co-adsorbents. This may allow the substrate to access the reaction sites more freely, thereby altering the interaction geometry. Consequently, the preferred direction of hydrogen addition may be reversed, leading to a change in enantioselectivity. The importance of multidentate adsorption and molecular flexibility in organic modifiers has also been demonstrated in the shape-controlled growth of TiO_2 single crystals, where organic molecules bearing multiple functional groups can strongly interact with surface Ti sites and stabilize specific surface structures [20]. Previous spectroscopic studies have reported that TIO-13 exhibits relatively stable and well-defined surface states under photocatalytic conditions [21], which is consistent with the higher and more reproducible enantioselectivity observed for TIO-13 in the present study. Taken together, these results suggest, rather than conclusively prove, that relatively ordered and less distorted TiO_2 surface structures are advantageous for enhancing enantioselectivity in chiral co-adsorbent-assisted photohydrogenation reactions. Because the present study is based on commercially available TiO_2 powders, the correlation between specific exposed facets and

stereochemical outcomes should be regarded as a structure–property interpretation, and further studies using facet-controlled TiO_2 crystals will be required for definitive verification.

4. Conclusions

In this study, enantioselective photohydrogenation of aromatic ketones was systematically investigated using TiO_2 photocatalysts in the presence of chiral co-adsorbents. Chiral aromatic hydroxylamines, such as PhEA, were found to act as effective and stable co-adsorbents, providing moderate enantioselectivity with significantly reduced inhibition compared with carboxylate-type co-adsorbents such as MA. Detailed structural analyses of anatase TiO_2 photocatalysts revealed that crystal morphology, particle size, and exposed facets are closely related to both photocatalytic activity and enantioselectivity. Anatase TIO-13, possessing relatively large particles with more well-defined crystal facets, exhibited higher and more reproducible enantioselectivity, whereas TIO-7, composed of smaller nanoparticles with lattice distortion and heterogeneous facet exposure, showed higher reaction rates but lower enantioselectivity. The inverse relationship observed between reaction rate and enantioselectivity suggests that excessive surface heterogeneity and lattice distortion weaken the cooperative interactions between chiral co-adsorbents and substrate molecules on the TiO_2 surface. These findings highlight the importance of ordered surface structures and well-defined adsorption geometries for achieving efficient asymmetric induction in heterogeneous photocatalysis. At the same time, the present work should be regarded primarily as a fundamental study rather than a practically optimized catalytic methodology, because the substrate scope remains limited and the enantioselectivities remain moderate under conditions that afford acceptable product yields. Within these limitations, the present results suggest that control of TiO_2 crystal structure, in combination with rational design of chiral co-adsorbents, is a promising strategy for enhancing enantioselectivity in semiconductor-based asymmetric photocatalytic reactions. Further mechanistic, spectroscopic, and facet-controlled studies will be necessary to establish the detailed origin of asymmetric induction and to expand the generality of this catalytic concept.

Supplementary Materials

The following supporting information can be found at: https://www.sciepublish.com/article/pii/1000, Figure S1: Time profile of concentration ratio ($C/C_0 \times 100\%$) where C and C_0 are the concentration of (*S*)-PhEA at each reaction time and 0 h, respectively during the photohydrogenation of **2a** to **2b**. Figure S2: Optimized molecular structures and calculated charge distributions of four chiral co-adsorbents obtained by density functional theory (DFT) calculations using the Gaussian program. Figure S3: Time courses of (a) yield and (b) enantiomeric excess (*ee*) during two consecutive enantioselective photohydrogenation experiments. Reaction conditions: TiO_2 (TIO-13), substrate (2NP), and chiral co-adsorbent ((*S*)-PhEA). Figure S4: TEM images and corresponding particle size distributions of four TiO_2 samples. Representative TEM images of P25, TIO-6, TIO-7, and TIO-13 are shown together with the particle size distributions obtained by statistical analysis of the TEM images. Figure S5: Schematic illustrations of representative anatase TiO_2 particle morphologies and exposed crystal facets discussed in this study. Figure S6: Bulk-cut atomic models, top-view representations, and corresponding STEM observations of the anatase TiO_2 (112) surface. Table S1: Comparison of yield, *ee*, and inhibition ratio (*IR*) between a single experiment and repeated experiments (1st and 2nd irradiations). Reaction conditions: TiO_2 (TIO-13), substrate (2NP), and chiral co-adsorbent ((*S*)-PhEA). Table S2: XRD data for anatase TiO_2 samples TIO-13 and TIO-7. The table lists the diffraction angles (2θ), corresponding Miller indices (*hkl*), peak intensities, and integrated peak areas for each sample. Table S3: Comparison of initial reaction rates ($mmol \cdot L^{-1} \cdot h^{-1}$) for the photohydrogenation of substrates **1a** (1NP) and **2a** (2NP) over four TiO_2 photocatalysts. The initial rates were measured in the absence of a chiral co-adsorbent and in the presence of MA or PhEA as chiral co-adsorbents.

Statement of the Use of Generative AI and AI-Assisted Technologies in the Writing Process

During the preparation of this manuscript, the authors used ChatGPT (OpenAI) in order to improve the clarity and readability of the English text. After using this tool, the authors reviewed and edited the content as needed and take full responsibility for the content of the published article.

Acknowledgments

The authors are grateful to Y. Miura and S. Kawashima for their helpful experimental assistance.

Author Contributions

Conceptualization, A.K., H.M. and S.K.; Methodology, A.K. and K.H.; Software, A.K. and K.H.; Validation, A.K.; Formal Analysis, A.K. and K.H.; Investigation, A.K. and S.K.; Resources, A.K. and S.K.; Data Curation, A.K. and S.K.; Writing—Original Draft Preparation, A.K., H.M. and S.K.; Writing—Review & Editing, H.M.; Visualization, A.K. and H.M.; Supervision, H.M. and S.K.; Project Administration, H.M. and S.K.; Funding Acquisition, H.M. and S.K.

Ethics Statement

Not applicable.

Informed Consent Statement

Not applicable.

Data Availability Statement

The data supporting this study are available upon reasonable request.

Funding

This work was supported by JSPS KAKENHI Grant-in-Aid for Scientific Research (C) Grant Number19K05681 (to S.K.) and 20K06954 (to H.M.).

Declaration of Competing Interest

The authors declare that they have no known competing financial interests or personal relationships that could have appeared to influence the work reported in this paper.

References

1. Li YH, Zhe H, Li YJ, Song XY, Duan YY, Zhang Y, et al. Asymmetric Chiral Photocatalysts. *ACS Catal.* **2025**, *15*, 7543–7577. DOI:10.1021/acscatal.5c00273
2. Li S, Xu XX, Xu LG, Lin HW, Kuang H, Xu CL. Emerging trends in chiral inorganic nanomaterials for enantioselective catalysis. *Nat. Commun.* **2024**, *15*, 3506. DOI:10.1038/s41467-024-47657-y
3. Qiu XY, Zhang Y, Zhu YF, Long CL, Su LN, Liu SQ, et al. Applications of Nanomaterials in Asymmetric Photocatalysis: Recent Progress, Challenges, and Opportunities. *Adv. Mater.* **2021**, *33*, 2001731. DOI:10.1002/adma.202001731
4. Kohtani S, Kawashima A, Miyabe H. Stereoselective Organic Reactions in Heterogeneous Semiconductor Photocatalysis. *Front. Chem.* **2019**, *7*, 630. DOI:10.3389/fchem.2019.00630
5. Kohtani S, Yoshioka E, Saito K, Kudo A, Miyabe H. Photocatalytic hydrogenation of acetophenone derivatives and diaryl ketones on polycrystalline titanium dioxide. *Catal. Commun*. **2010**, *11*, 1049–1053. DOI:10.1016/j.catcom.2010.04.022
6. Kohtani S, Kamoi Y, Yoshioka E, Miyabe H. Kinetic study on photocatalytic hydrogenation of acetophenone derivatives on titanium dioxide. *Catal. Sci. Technol.* **2014**, *4*, 1084–1091. DOI:10.1039/c3cy00879g

7. Kohtani S, Kawashima A, Masuda F, Sumi M, Kitagawa Y, Yoshioka E, et al. Chiral α-hydroxy acid-coadsorbed TiO_2 photocatalysts for asymmetric induction in hydrogenation of aromatic ketones. *Chem. Commun.* **2018**, *54*, 12610–12613. DOI:10.1039/c8cc07295g
8. Liu G, Yang HG, Pan J, Yang YQ, Lu GQ, Cheng H-M. Titanium Dioxide Crystals with Tailored Facets. *Chem. Rev.* **2014**, *114*, 9559−9612. DOI:10.1021/cr400621z
9. Roy N, Sohn Y, Pradhan D. Synergy of Low-Energy {101} and High-Energy {001} TiO_2 Crystal Facets for Enhanced Photocatalysis. *ACS Nano* **2013**, 7, 2532–2540. DOI:10.1021/nn305877v
10. Lee T-Y, Lee C-Y, Chiu H-T. Enhanced Photocatalysis from Truncated Octahedral Bipyramids of Anatase TiO_2 with Exposed {001}/{101} Facets. *ACS Omega* **2018**, *3*, 10225–10232. DOI:10.1021/acsomega.8b01251
11. Joutsuka T, Yoshinari H, Yamauchi S. Facet Dependence of Photocatalytic Activity in Anatase TiO_2: Combined Experimental and DFT Study. *Bull. Chem. Soc. Jpn.* **2021**, *94*, 106–111. DOI:10.1246/bcsj.20200236
12. Tseng C-L, Chen Y-K, Wang S-H, Peng Z-W, Lin J-L. 2-Ethanolamine on TiO_2 Investigated by *In Situ* Infrared Spectroscopy Adsorption. *J. Phys. Chem. C* **2010**, *114,* 11835–11843. DOI:10.1021/jp9117166
13. Parameswari A, Soujanya Y, Sastry GN. Functionalized Rutile TiO_2(110) as a Sorbent To Capture CO_2 through Noncovalent Interactions: A Computational Investigation. *J. Phys. Chem. C* **2019**, *123*, 3491−3504. DOI:10.1021/acs.jpcc.8b09311
14. Warren D, Shapira Y, Kisch H, McQuillan AJ. Apparent Semiconductor Type Reversal in Anatase TiO_2 Nanocrystalline Films. *J. Phys. Chem. C* **2007**, *111*, 14286−14289. DOI:10.1021/jp0753934
15. Bertolotti F, Vivani A, Moscheni D, Ferri F, Cervellino A, Masciocchi N, et al. Structure, Morphology, and Faceting of TiO_2 Photocatalysts by the Debye Scattering Equation Method. The P25 and P90 Cases of Study. *Nanomaterials* **2020**, *10*, 743. DOI:10.3390/nano10040743
16. Wallace SK, McKenna KP. Facet-Dependent Electron Trapping in TiO_2 Nanocrystals. *J. Phys. Chem. C* **2015**, 119, 1913–1920. DOI:10.1021/jp511529u
17. Mino L, Spoto G, Bordiga S, Zecchina A. Particles Morphology and Surface Properties as Investigated by HRTEM, FTIR, and Periodic DFT Calculations: From Pyrogenic TiO_2(P25) to Nanoanatase. *J. Phys. Chem. C* **2012**, *116*, 17008–17018. DOI:10.1021/jp303942h
18. Murakami N, Mahaney OOP, Abe R, Torimoto T, Ohtani B. Double-Beam Photoacoustic Spectroscopic Studies on Transient Absorption of Titanium(IV) Oxide Photocatalyst Powders. *J. Phys. Chem. C* **2007**, *111*, 11927–11935. DOI:10.1021/jp071362x
19. Wu Y, Gao F, Wang H, Kovarik L, Sudduth B, Wang Y. Probing Acid−Base Properties of Anatase TiO_2 Nanoparticles with Dominant {001} and {101} Facets Using Methanol Chemisorption and Surface Reactions. *J. Phys. Chem. C* **2021**, *125*, 3988−4000. DOI:10.1021/acs.jpcc.0c11107
20. Yang S, Yang BX, Wu L, Li YH, Liu P, Zhao H, et al. Titania Single Crystals with a Curved Surface. *Nat. Commun.* **2014**, *5*, 5355. DOI:10.1038/ncomms6355
21. Savory DM, McQuillan AJ. Influence of Formate Adsorption and Protons on Shallow Trap Infrared Absorption (STIRA) of Anatase TiO_2 During Photocatalysis. *J. Phys. Chem. C* **2013**, *117*, 23645−23656. DOI:10.1021/jp404321f